ACS APPLIED MATERIALS & INTERFACES

Research Article

www.acsami.org

Predicting Vertical Phase Segregation in Polymer-Fullerene Bulk Heterojunction Solar Cells by Free Energy Analysis

Michael D. Clark,[†] Michael L. Jespersen,[‡] Romesh J. Patel,[†,§] and Benjamin J. Leever[†,*]

[†]Materials and Manufacturing Directorate, Air Force Research Laboratory, Wright-Patterson AFB, Ohio 45433

[‡]University of Dayton Research Institute, 300 College Park, Dayton, Ohio 45469

[§]UES Inc., 4401 Dayton-Xenia Road, Dayton, Ohio 45432

Supporting Information

ABSTRACT: Blends of poly(3-hexylthiophene) (P3HT) and C_{61}-butyric acid methyl ester (PCBM) are widely used as a model system for bulk heterojunction active layers developed for solution-processable, flexible solar cells. In this work, vertical concentration profiles within the P3HT:PCBM active layer are predicted based on a thermodynamic analysis of the constituent materials and typical solvents. Surface energies of the active layer components and a common transport interlayer blend, poly(3,4-ethylenedioxythiophene) poly(styrenesulfonate) (PEDOT:PSS), are first extracted using contact angle measurements coupled with the acid–base model. From this data, intra- and interspecies interaction free energies are calculated, which reveal that the thermodynamically favored arrangement consists of a uniformly blended "bulk" structure capped with a P3HT-rich air interface and a slightly PCBM-rich buried interface. Although the "bulk" composition is solely determined by P3HT:PCBM ratio, composition near the buried interface is dependent on both the blend ratio and interaction free energy difference between solvated P3HT and PCBM deposition onto PEDOT:PSS. In contrast, the P3HT-rich overlayer is independent of processing conditions, allowing kinetic formation of a PCBM-rich sublayer during film casting due to limitations in long-range species diffusion. These thermodynamic calculations are experimentally validated by angle-resolved X-ray photoelectron spectroscopy (XPS) and low energy XPS depth profiling, which show that the actual composition profiles of the cast and annealed films closely match the predicted behavior. These experimentally derived profiles provide clear evidence that typical bulk heterojunction active layers are predominantly characterized by thermodynamically stable composition profiles. Furthermore, the predictive capabilities of the comprehensive free energy approach are demonstrated, which will enable investigation of structurally integrated devices and novel active layer systems including low band gap polymers, ternary systems, and small molecule blends.

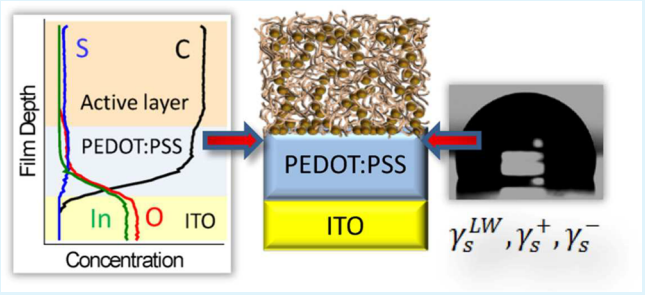

KEYWORDS: *P3HT:PCBM bulk heterojunction, surface energy, free energy, X-ray photoelectron spectroscopy, polymer solar cell*

INTRODUCTION

Organic electronics such as organic photovoltaics (OPVs) and light-emitting diodes (OLEDs) have received significant attention in recent years as promising candidate materials for next generation energy harvesting, power generation, flexible displays, and solid state lighting.[1,2] State of the art organic devices employ a semiconducting polymer heterojunction sandwiched between a transparent and a metallic electrode, oftentimes including charge selective interfacial materials.

Among the most explored OPV device architectures is the bulk heterojunction (BHJ), which consists of a bicontinuous interpenetrating network of an electron donor–acceptor blend, where poly(3-hexylthiophene) (P3HT) and C_{61}-butyric acid methyl ester (PCBM) comprise the most widely studied pair.[1,2] Ideally, the blend domain size should approach the exciton diffusion length (~10 nm) to reduce charge recombination while maximizing the acceptor–donor interfacial area where charge separation occurs.[3] Furthermore, pathway continuity to the appropriate electrode is essential for maximizing charge extraction and therefore, device efficiency. Such considerations necessitate precise control over nanoscale morphology and vertical stratification of the active layer components. OPV device design is further complicated by the inclusion of additional layers such as poly(3,4-ethylenedioxythiophene) poly(styrenesulfonate) (PEDOT:PSS) to improve device efficiency and modify work function.[4] As these interfacial and active layers are sequentially solution-cast onto one another, control of the developing nanostructure requires a clear understanding of the roles of surface energy and interfacial interactions. These considerations, along with annealing conditions, are crucial for maximizing device performance.

Received: January 28, 2013
Accepted: May 20, 2013
Published: May 20, 2013

   dx.doi.org/10.1021/am4003777 | *ACS Appl. Mater. Interfaces* 2013, 5, 4799–4807

Recent reports have examined the vertical stratification and interfacial blend compositions of OPV devices using spectroscopic ellipsometry,[5,6] electron tomography[7,8] and microscopy,[9] X-ray[10] and neutron reflectivity,[11] near-edge X-ray absorption fine structure,[6,12−14] and depth profiling using X-ray photoelectron spectroscopy (XPS),[15,16] Auger electron spectroscopy,[17] or time-of-flight ion mass spectroscopy.[16,18,19] Our understanding of nanostructure development is still limited, however, because these reports have yielded conflicting results. For example, several groups found a nearly 50:50 P3HT:PCBM blend decorated the buried interface of an annealed P3HT:PCBM film,[5,6,16] whereas other researchers detected PCBM-rich[11,14,15,20] or P3HT-rich compositions.[7,12,13] Annealing effects on concentration gradients and interface compositions have also been unclear, with groups suggesting both enhanced[7,10,12,20] and suppressed[5,11,16] concentration gradients after annealing. Furthermore, these studies have provided limited insight into the fundamental origin of emerging concentration gradients, specifically whether they are attributable to kinetic limitations on long-range species diffusion or are thermodynamically stable.

In light of these contradictory reports, we present a coupled theoretical and experimental approach to examining network development in bulk heterojunction solar cells using the model P3HT:PCBM blend as a basis. In this work, for the first time, interaction free energies of the device constituents are determined using surface energy analysis as extrapolated from contact angle measurements. Using these results, a fundamental understanding of the thermodynamic driving force for phase segregation and interspecies interactions is presented, which allows prediction of composition profiles within the blended films. Vertical stratification in a series of P3HT:PCBM blends is then examined as a function of annealing conditions and blend ratio using angle-resolved X-ray photoelectron spectroscopy (ARXPS) and XPS depth profiling. Strong correlations emerge between the predicted behavior and XPS results, indicating that the detected vertical stratification within the P3HT:PCBM blend is dominated by thermodynamic equilibrium rather than kinetic limitations. In addition, the predictive capacity of the comprehensive free energy approach is validated, suggesting its utility in examining other studied systems including low band gap polymers and ternary blends.

EXPERIMENTAL SECTION

Materials. Indium tin oxide (ITO) coated aluminosilicate glass substrates (10 Ω $\square^{-1}$) were purchased from Colorado Concept Coatings, while the PEDOT:PSS aqueous dispersion (Clevios P, 1.2−1.4% solids, 60−100 mPa s viscosity, < 1 M Ω $\square^{-1}$) was purchased from Heraeus. P3HT (M_w ≈ 50−70k, PDI ∼ 1.6−1.8, 91−94% regioregular, < 0.01% metal) and PCBM (99.5% fullerene) were procured from Rieke Metals, Inc. and American Dye Source respectively. Glass slides and polycarbonate (PC) resin pellets (Mw ∼ 45−60k) were obtained from Fisher Scientific and Scientific Polymer Products. Micro-90 detergent solution was purchased from Cole-Parmer. All solvents including anhydrous chlorobenzene (CB) and 1,2-dichlorobenzene (DCB) were purchased from Sigma Aldrich and used without further purification while distilled (DI) water was extracted from an in-house purification system.

Multilayer Film Construction. ITO coated glass substrates were degreased ultrasonically for 20 min in sequential baths of detergent solution (5 vol %), DI water, hexanes, isopropanol, acetone, and methanol before drying under flowing nitrogen. Degreased substrates were then UV-ozone (UVO) treated for 20 min before placing PEDOT:PSS droplets onto the ITO substrate after passing through a 0.45 μm PVDF syringe filter (Millipore). PEDOT:PSS was then spin cast at 3500 rpm for 45 s with a 3 s ramp and baked at 160 °C on a hot plate for 15 min to give 80 ± 5 nm films. In a N_2 glovebox, active layer dispersions were prepared in CB (15 mg/mL for pure P3HT and PCBM, or 24 mg/mL for P3HT:PCBM blends) with the desired weight ratio followed by overnight stirring at 60 °C in an oil bath. Active layer dispersion droplets were then passed through a 0.45 μm PTFE syringe filter (Millipore) before adding onto the PEDOT:PSS coated ITO substrates. Active layer films were subsequently spin cast at 1500 rpm for 45 s with a 3 s ramp before annealing (if needed) at 160 °C in a glovebox oven for 8 min.

To further verify PEDOT:PSS film surface energy, PEDOT:PSS layers were also cast at 1500 rpm for 45 s with a 6 s ramp to generate thicker films (154.0 ± 5.7 nm). These thicker films were cast on both UVO treated ITO and PC coated glass slides. The latter were prepared by cleaning glass slides using the ITO protocol described above before spin casting PC from chloroform (5 wt %) at 500 rpm for 45 s with a 6 s ramp and baking at 160 °C on a hot plate for 15 min. The PC coating was then UVO treated for 10 min to enhance wettability before casting the PEDOT:PSS film as described previously.

Characterization. Tapping mode atomic force microscopy (AFM) images were taken using a Dimension Instruments Dimension 3100 equipped with silicon tips (Nanosensors) scanning at 0.5−1.0 Hz. Roughness averages were calculated by examining 3 different substrates with 3 images collected per film. Layer thickness was assessed by optical profilometry (KLA Tencor P15) after scoring the surface with a fresh razor with 6 measurements per substrate. Cross-section transmission electron microscopy (TEM) images were taken in bright field mode using a Philips CM200 LaB6 microscope operating at 200kV.

Cross-sectioned foils were prepared by loading prefabricated films into a focused ion beam (FIB) apparatus equipped with scanning electron microscopy (SEM) capabilities for monitoring ion beam etching. A protective Pt cap was deposited from a standard organometallic precursor using sequential electron and ion beam deposition. The foil was then ion etched on both sides of the cap in successive steps of smaller aperture sizes to smooth surface roughness. After prelift out cuts were made, the foil was attached to the Omniprobe using a Pt bridge before transferring onto a TEM grid. Final thinning was then performed to ensure electron transparency.

Wettability Measurements. Contact angle measurements were collected on a VCA Optima (AST Products) where 3 μL droplets were applied to the surface and left equilibrating for 15 s before measuring the advancing contact angle (θ_{adv}). The equilibration time was selected as the time needed for a nonabsorbing, highly wetting liquid to yield a stable contact angle (e.g., diiodomethane on UVO ITO). Afterward, 0.5 μL were retracted before waiting an additional 15 s for receding angle measurements (θ_{rec}). A minimum of 10 droplets were measured for each liquid−solid combination with outliers being removed, giving at least 8 measurements for averaging.

XPS Measurements. XPS was performed on a Kratos Axis Ultra spectrometer using a monochromatic Al K_α radiation source (1486.6 eV), where the emission current and operating voltage were fixed at 10 mA and 12 kV for all experiments. Angle resolved survey spectra were collected in hybrid lens mode using 160 eV pass energy in the 0−1200 eV range with a 1 eV step size and dwell time of 1 s. The spot size was fixed at approximately 300 μm x 700 μm (0.21 mm^2), whereas the photoelectron emission angle was varied from 0 to 75°. Depth profiling experiments were performed using an Ar^+ sputtering gun operated at 500 V, rastering a 1.5 × 1.5 mm^2 area with 15 and 10 s pre- and post-etch delays. The sampling spot size was further reduced to 9.5 × 10^{-3} mm^2 to minimize edge effects. Survey spectra were collected as described above except the energy window and dwell time were 0−600 eV and 0.5 s, respectively. High resolution S 2p scans were collected using 40 eV pass energy between 156 and 176 eV with a 0.2 eV step size and a 2 s dwell time. Collected spectra were fitted using Gaussian−Lorentzian peaks after Shirley background subtraction.

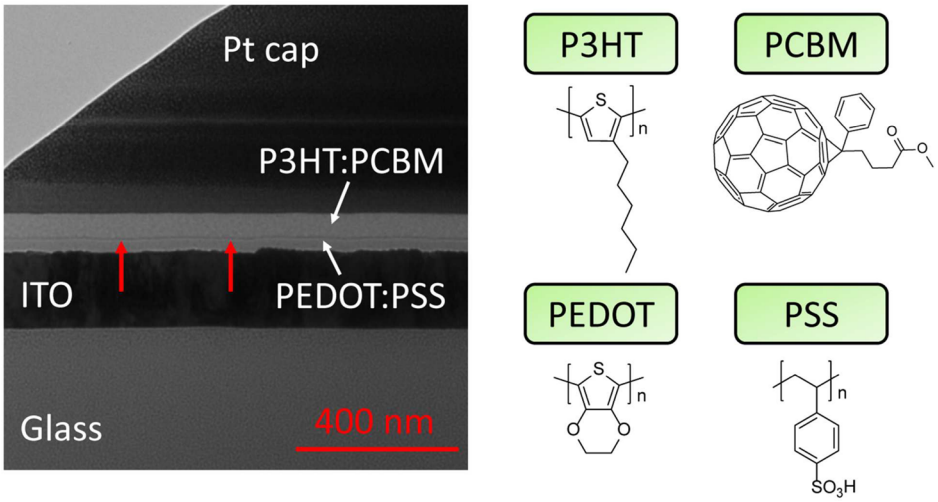

Figure 1. TEM image of an annealed OPV film cross-section capped with a protective Pt layer. The image was defocused (−10 μm) to enhance the P3HT:PCBM/PEDOT:PSS interface (red arrows). The chemical structures of the active layer (P3HT and PCBM) and interlayer (PEDOT and PSS) blend components are also illustrated.

Table 1. Advancing Contact Angle (θ_{adv}) and Contact Angle Hysteresis ($\Delta\theta$) of Test Liquids on the Different Surfaces Examined in This Study

	test liquid							
	diiodomethane		water		formamide		glycerol	
	θ_{adv}	$\Delta\theta$	θ_{adv}	$\Delta\theta$	θ_{adv}	$\Delta\theta$	θ_{adv}	$\Delta\theta^a$
				Substrates				
UVO ITO	26.0 ± 1.8	5.5 ± 2.5	9.5 ± 1.0	1.9 ± 0.7	6.6 ± 0.9	0.5 ± 0.4	13.6 ± 2.5	
PEDOT:PSS	24.8 ± 1.5	4.1 ± 1.2	8.5 ± 2.9	1.8 ± 2.1	[b]	[b]	18.7 ± 1.5	
				Active Layer Films[c]				
P3HT:PCBM (5:3 annealed)	69.8 ± 1.4	6.3 ± 2.6	106.7 ± 1.0	4.3 ± 1.3	90.1 ± 1.3	6.7 ± 2.4	95.5 ± 1.2	
P3HT:PCBM[d] (5:3 annealed)	68.2 ± 1.9	7.6 ± 1.6	107.6 ± 0.5	6.5 ± 1.2	90.3 ± 1.4	4.3 ± 2.7	95.5 ± 1.0	
P3HT:PCBM (5:3 as cast)	68.8 ± 2.4	7.7 ± 2.0	106.3 ± 1.1	5.5 ± 0.9	89.5 ± 0.8	4.2 ± 3.2	94.7 ± 0.9	
P3HT:PCBM (3:5 annealed)	68.9 ± 2.0	8.6 ± 3.4	106.8 ± 1.1	2.7 ± 1.5	89.2 ± 2.0	5.9 ± 1.8	95.0 ± 1.1	
P3HT:PCBM (3:5 as cast)	65.5 ± 4.5	7.9 ± 1.7	106.3 ± 1.1	6.4 ± 1.7	91.0 ± 2.7	6.9 ± 1.5	93.8 ± 1.0	
P3HT only	66.3 ± 1.6	5.4 ± 2.5	106.8 ± 0.6	3.6 ± 1.4	89.4 ± 1.2	1.7 ± 1.2	96.0 ± 0.8	
PCBM only	11.3 ± 2.8		89.7 ± 3.0	7.6 ± 2.7	65.3 ± 4.9	8.3 ± 2.9	74.9 ± 1.7	

[a]Receding angle measurements unreliable due to glycerol's high viscosity. [b]Advancing contact angle ≤ 5°. [c]Depicted active layer films spin cast from CB dispersion unless otherwise noted. [d]Active layer spin cast from DCB dispersion.

RESULTS AND DISCUSSION

Film Fabrication. Though numerous recent reports have explored OPV device performance optimization through solvent selection,[21,22] blend concentration ratios,[8,23,24] and annealing conditions,[18,25,26] the influence of such parameters on vertical concentration profiles within the active layer remains unclear due to the numerous contradictory reports found in literature.[5,10−12,15,16] To investigate these variables, we fabricated a series of P3HT:PCBM films using the typical P3HT:PCBM/PEDOT:PSS/ITO architecture (Figure 1), where PEDOT:PSS and P3HT:PCBM were successively spin-cast onto the precleaned ITO substrates. In addition to the P3HT:PCBM blends, pure P3HT and PCBM films were also cast to serve as reference samples.

Layer Wettability. To provide a theoretical basis for composition profiles within P3HT:PCBM films, contact angle measurements were performed on fabricated P3HT, PCBM, and P3HT:PCBM surfaces using a series of well-characterized, high energy solvents. These measurements, when coupled with an appropriate surface energy model, allow extraction of surface energy components of the substrate, PEDOT:PSS interlayer, and active layer constituents, which in turn predict the favored thermodynamic structure of the multilayered films. The measured advancing angle (θ_{adv}) and contact angle hysteresis ($\Delta\theta \equiv \theta_{adv} - \theta_{rec}$) data are recorded in Table 1, where the latter is correlated with inherent surface roughness. From the data, it is clear that measured $\Delta\theta$ of the UVO ITO substrates are similar to other surfaces despite ITO's enhanced surface roughness ($r_{RMS} \approx 5$ nm). However, in the roughness wetting (i.e., Wenzel) regime, microscale roughness is needed to produce appreciable $\Delta\theta$ variation.[27] In addition, α-bromonaphthalene ($\gamma_L = 44.4$ mJ/m^2) was considered as a probe liquid but was found to wet both PEDOT:PSS and UVO ITO, while displaying evidence of wicking and P3HT dissolution on active layer surfaces. Thus, its usage was deemed unreliable for assessing surface energy.

It should be noted that the diiodomethane contact angle on pure PCBM films continuously evolved throughout the experiment, undergoing a decrease-increase cycle before reaching a plateau. Thus, droplet images were collected every 5 s to evaluate contact angle evolution over time, where the minimum contact angle was considered to be the actual angle.

Several of these time-dependent droplet tracks are shown in the Supporting Information. This selection of the minimum contact angle contrasts a recent report on C_{60} surface energy, where the initial contact angle was selected to reduce solvent wicking effects.[28] However, we assume that reaching droplet equilibrium takes several seconds on any partially wetted surface. Nevertheless, selecting the initial contact angle yielded only slight variation in measured contact angle (17.6 ± 2.7°), which led to negligible changes in extracted surface energy parameters. Similarly, water droplets on ITO and PEDOT:PSS surfaces were likewise allowed to equilibrate before measuring contact angles.

Although UVO ITO and PEDOT:PSS were observed to be hydrophilic, active layer surfaces displayed characteristic hydrophobic behavior, with PCBM and P3HT surfaces exhibiting water contact angles comparable to graphite (86°) and Teflon (110°).[29] The P3HT and blend surfaces were also characterized by large contact angles with the remaining probe liquids indicating low energy surfaces. Furthermore, the fabricated blend films displayed contact angles similar to pure P3HT despite changes in blend ratio, dispersing media, and thermal annealing, indicating that the blend films are capped with a P3HT-rich surface in agreement with other reports.[12,13,15,16,20,30] This observation was further corroborated by tapping-mode AFM phase images (Figure 2), where blend films retained a fibrous surface morphology similar to the pure P3HT film. Sporadic dark spots are also featured in the blend films (red circles), which are attributed to sparse PCBM clusters at the exposed surface.

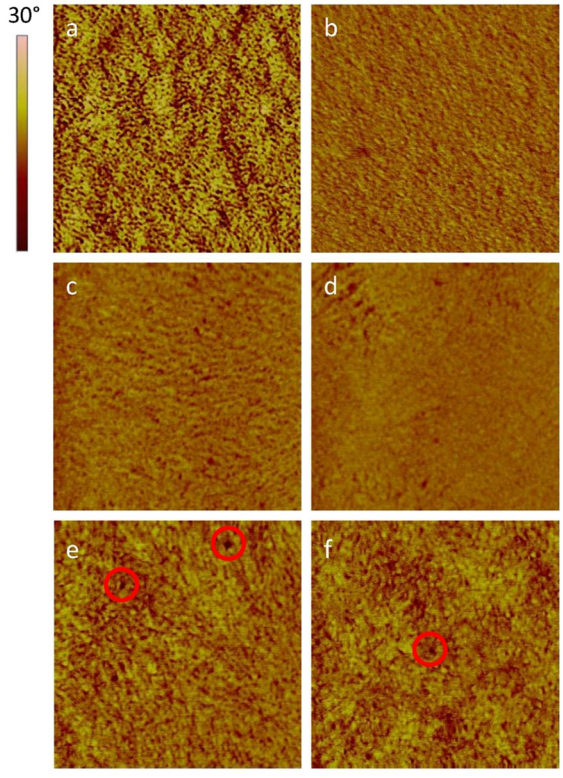

Figure 2. Tapping mode AFM phase images of (a) P3HT, (b) PCBM, and P3HT:PCBM blends deposited onto PEDOT:PSS coated ITO substrates. P3HT:PCBM images feature the 5:3 ratio (c) as-cast and (e) annealed films as well as the 3:5 blend (d) as-cast and (f) annealed surfaces. The images are 1 μm × 1 μm.

Surface Energy Calculation. To evaluate surface energy components, we utilized advancing contact angle measurements to produce 1000 data sets with a normal distribution based on the measured standard deviation (see the Supporting Information). Surface energy components were extracted from each data set with a fitting routine based on the acid–base model,[31] which is given by

$$(1 + \cos\theta_{adv})\gamma_L^T = 2\left(\sqrt{\gamma_S^{LW}\gamma_L^{LW}} + \sqrt{\gamma_S^+\gamma_L^-} + \sqrt{\gamma_S^-\gamma_L^+}\right), \quad (1)$$

where γ^T, γ^{LW}, γ^+, and γ^- denote the total, Lifshitz-van der Waals (dispersive), Lewis acid and base surface energy components, while the subscripts S and L refer to the solid surface and probe liquid. Thus, full description of an unknown surface requires contact angle measurements using at least three well-characterized probe liquids, one of which must be purely dispersive (i.e., apolar). A theoretical overview of the acid–base model and accompanying surface energy components for the probe liquids is provided in the Supporting Information. The results of the data fitting are shown in Table 2, where it is noted that data from the four probe liquids were used simultaneously for component assessment. While numerous ITO surface energy reports favor two parameter models such as the harmonic[32,33] and geometric mean theory,[34−36] these models are unable to account for negative mixing enthalpies, which determine solubility of water soluble polymers such as PEDOT:PSS.[31] Consequently, the acid–base model has been used to examine polymers,[37,38] biomolecules,[39] fullerenes,[40,41] and inorganic thin films,[42] and thus was used in this study.

Although the extracted PCBM surface energy matches well with carbon nanotube[41] and C_{60} reports,[40] assessment of PEDOT:PSS and P3HT surface energy components reveals some contrast with reported values. Most notably, Wang et al.[43] reported slightly higher polar components for P3HT, whereas PEDOT:PSS featured a reduced dispersive component and elevated Lewis base component when compared with our current findings. However, their procedure involved contact angles measured using the in situ Wilhelmy technique with hexadecane, ethylene glycol, and water as probe liquids. It is well established that measurement technique and probe liquid selection influence tabulated surface energy parameters so some discrepancy is expected, particularly when utilizing low energy solvents on hydrophobic surfaces (e.g., hexadecane on P3HT). For example, γ^+ in C_{60} compressed pellets increased from 0 to 3.1 mJ/m^2 simply by exchanging the selected apolar liquid.[40] In an effort to minimize probe liquid combination dependence, surface energy components were extracted using contact angle results from the four high energy liquids simultaneously. This approach curbs the intrinsic component sensitivity associated with select liquid combinations while addressing scatter within the contact angle data. Further explanation may be found in the Supporting Information. It is also worth mentioning that the extracted PEDOT:PSS and UVO ITO surface energies were remarkably similar, suggesting the possibility of contact angles probing ITO spikes rather than the PEDOT:PSS surface. To alleviate this concern, thicker PEDOT:PSS layers were cast onto both UVO ITO and PC coated glass (42.0 ± 0.7, 3.40 ± 0.33, and 33.3 ± 3.1 mJ/m^2 for dispersive, Lewis acid and base components). However, contact angle variability between the different PEDOT:PSS coated substrates was minimal, ensuring accurate detection of PEDOT:PSS surface energy, which was consistent with literature values (47–71 mJ/m^2).[43−45]

Table 2. Fitted surface energy parameters for OPV device constituents assessed through simultaneous fitting of diiodomethane, water, glycerol, and formamide contact angle data (when applicable).

	surface energy parameters (mJ/m^2)				
	γ^T	γ^{LW}	γ^{AB}	γ^+	γ^-
UVO ITO	61.0 ± 2.7	45.6 ± 1.4	15.4 ± 1.3	1.22 ± 0.21	48.8 ± 0.6
PEDOT:PSS	63.1 ± 2.8	44.6 ± 2.8	18.5 ± 2.1	1.86 ± 0.20	46.2 ± 1.5
P3HT[a]	23.2 ± 0.6	23.2 ± 0.6	[b]	[b]	0.31 ± 0.12
PCBM	45.1 ± 1.7	45.1 ± 1.7	[b]	[b]	0.88 ± 0.69

[a]P3HT:PCBM blend surfaces exhibited surface energy components within standard deviation of the pure P3HT surface. [b]Surface energy component found to be negligible.

It is important to note that P3HT:PCBM blends had characteristic surface energies similar to those measured for pristine P3HT films, confirming that a P3HT-rich interface decorates the exposed surface. Varying the P3HT:PCBM ratio, substituting chlorinated dispersing media (e.g., DCB), and thermal annealing did little to augment measured surface energy, indicating that P3HT migration to the exposed surface was completed during spin casting and is independent of blend ratio and chlorinated dispersing media. This rapid in situ formation of a P3HT-rich capping layer contrasts a recent report[10] but, is consistent with several other reports[11,12,16,20,26,30] suggesting some sensitivity to preparation technique. Thus, blend casting readily fabricates a thermodynamically air stable surface, indicating that other processing factors likely influence crystallization and species diffusion in the "bulk" film rather than phase migration at the exposed surface, which is consistent with the AFM imaging (Figure 2). Although Chen et al.[26] detected some P3HT crystallite reorientation during blend annealing, the authors found that the (100) reflection (i.e., edge-on) remained the dominant orientation after extended annealing, suggesting a limited impact on surface energy. It should be noted, however, that the exposed surface composition and behavior will vary when P3HT:PCBM films are heat treated after capping with another layer (e.g., Al cathode, encapsulation film).

Free Energy Analysis. To further explore the underlying thermodynamics governing species aggregation, we used surface energies to calculate the interaction free energies between constituents associated within the fabricated OPV structure. While Hamaker constants examine only dispersive interactions, the polar nature of PEDOT:PSS would be expected to dramatically influence intramolecular interactions within the present system. Consequently, free energy analysis must consider both polar and apolar molecular interactions between the dispersing media, active layer constituents (P3HT and PCBM), and the PEDOT:PSS interlayer. Using the acid–base model as a basis, the two- and three-body molecular interactions between the OPV constituents and dispersing media may be described using several equations. The free energy of adhesion between two molecular species (ΔG_{ij}) is given by:[31]

$$\Delta G_{ij} = -2\sqrt{\gamma_i^{LW}\gamma_j^{LW}} - 2\left(\sqrt{\gamma_i^+\gamma_j^-} + \sqrt{\gamma_i^-\gamma_j^+}\right), \quad (2)$$

which defines the ability of a solid particulate (1) to be solvated by a liquid molecule (3) or adhere in vacuo to a particulate of a different species (2).[31] The interaction free energy between two identical molecules immersed in a liquid (ΔG_{131}) is expressed as[31]

$$\Delta G_{131} = -2[(\sqrt{\gamma_1^{LW}} - \sqrt{\gamma_3^{LW}})^2 + 2(\sqrt{\gamma_1^+\gamma_1^-} + \sqrt{\gamma_3^+\gamma_3^-} - \sqrt{\gamma_1^+\gamma_3^-} - \sqrt{\gamma_1^-\gamma_3^+})], \quad (3)$$

whereas the energy between two different species (ΔG_{132}) is given by[31]

$$\Delta G_{132} = -2(\sqrt{\gamma_1^{LW}} - \sqrt{\gamma_3^{LW}})(\sqrt{\gamma_2^{LW}} - \sqrt{\gamma_3^{LW}}) + 2[(\sqrt{\gamma_1^+} - \sqrt{\gamma_2^+})(\sqrt{\gamma_1^-} - \sqrt{\gamma_2^-}) - (\sqrt{\gamma_1^+} - \sqrt{\gamma_3^+})(\sqrt{\gamma_1^-} - \sqrt{\gamma_3^-}) - (\sqrt{\gamma_2^+} - \sqrt{\gamma_3^+})(\sqrt{\gamma_2^-} - \sqrt{\gamma_3^-})]. \quad (4)$$

Although $\Delta G_{ij} < 0$ in all cases implies universal attraction, $\Delta G_{131} > 0$ defines favorable molecular dispersion of species (1) in media (3), whereas $\Delta G_{131} < 0$ implies aggregation of solvated molecules into clusters. In addition, $\Delta G_{132} > 0$ indicates a net repulsion between species (1) and (2) when dispersed in media (3), while $\Delta G_{132} < 0$ corresponds to interspecies aggregation within the liquid.

Using eqs 2–4, free energy calculations were made using the surface energy parameters in Table 2. These calculated values are given in the Supporting Information. From these calculations, several important conclusions can be drawn. First, although P3HT and PCBM show strong adhesion with chlorinated media, these constituents generally self-aggregate into clusters when dispersed in chlorinated solvents ($\Delta G_{131} < 0$). The only noted exception is P3HT, which is predicted to disperse into chloroform as individualized polymer chains ($\Delta G_{131} > 0$). Second, these clusters are predominately composed of pure species rather than blended aggregates, indicating that some phase segregation is present even in the dispersed state ($\Delta G_{132} > 0$). We also note stronger affinity of chlorinated solvents with PCBM rather than P3HT (e.g., $\Delta G_{13} = -55.5 \pm 0.9$ and -78.3 ± 2.1 for P3HT and PCBM solvated by CB), indicating that the solvent desorbs from P3HT (or P3HT "dries") more quickly than PCBM during spin casting. It has been reported that casting P3HT:PCBM from DCB increases P3HT crystallinity over comparable CB dispersions, which is attributed to slower solvent evaporation.[21] This is confirmed in our analysis, which shows stronger P3HT adhesion to DCB when compared with CB.

The most important findings of this energy analysis have to do with the vertical composition profiles within the active layer blend. A schematic highlighting the projected vertical stratification is depicted in Figure 3. Because P3HT surface energy is substantially less than PCBM, the exposed air surface would be almost exclusively composed of P3HT in agreement with our contact angle results as well as previous reports.[12,13,15,16,20] However, because the liquid dispersed

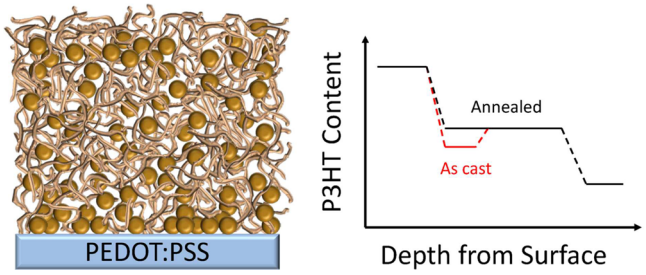

Figure 3. Predicted P3HT:PCBM blend vertical composition profiles based on surface energy analysis and free energy calculations.

blend is expected to be void of composition gradients, P3HT diffusion to the air surface during film casting remains localized, thereby creating a sublayer with an elevated PCBM concentration. This PCBM-rich sublayer is a kinetic construct of the rapid film drying process, which limits long-range species diffusion. As such, reduction of this PCBM-rich sublayer during annealing is expected. In the "bulk" film, however, active layer constituents are not influenced by either the air or buried interface, so its composition would correspond to initial blend concentration ratios (~58 and 33% P3HT for 5:3 and 3:5 P3HT:PCBM blends).

At the buried PEDOT:PSS interface, solvated P3HT and PCBM clusters preferentially begin interspecies aggregation due to the relatively small energetic penalty for such association (ΔG_{132} = 1.40 ± 0.93 for P3HT and PCBM solvated by CB), thereby beginning formation of the BHJ network before drying. Nevertheless, Chang et al.[46] recently demonstrated that P3HT:PCBM layers retain residual solvent after annealing, making it essential to retain solvent effects in any comprehensive free energy approach to quantify interfacial composition (i.e., ΔG_{132}). The energy barrier for solvated PCBM deposition onto the PEDOT:PSS surface is lower than for P3HT (ΔG_{132} = 7.93 ± 0.57 and 12.8 ± 0.34 for PCBM and P3HT immersed in CB respectively), while PCBM also shows stronger adhesion (ΔG_{12} = −94.9 ± 2.7 and −67.3 ± 1.2 for PCBM and P3HT). This phenomenon is independent of selected chlorinated solvent, indicating preferential PCBM decoration of the PEDOT:PSS interlayer. The relatively small energy barrier difference between solvated P3HT and PCBM deposition onto PEDOT:PSS suggests that the interfacial composition is not pure PCBM but instead will be a blended P3HT:PCBM mixture, the composition of which will be dictated by both the initial blend composition and free energy barrier ratio, which varies slightly with solvent selection. Taking the free energy barrier ratio into account in a simple first order approximation, 5:3 and 3:5 P3HT:PCBM blend films cast from CB are predicted to yield ~ 46 and 24% P3HT near the buried interface (see eq S8 in the Supporting Information). In contrast, the air surface is characterized by simultaneous P3HT-interface attraction and PCBM-interface repulsion ($\Delta G_{P3HT,CB,Air} < 0 < \Delta G_{PCBM,CB,Air}$). This suggests that P3HT will dominate surface composition, limited only by component mobility.

Vertical Stratification. To experimentally evaluate the theoretical calculations, vertical composition profiles in spin-cast and annealed P3HT:PCBM films were characterized using a combination of depth profiling XPS and ARXPS. Although ARXPS nondestructively resolves composition variation near the exposed surface, exploration of concentration gradients within the "bulk" film and near the buried PEDOT:PSS interface necessitates an in situ sputtering process. One drawback of sputtering is that ion bombardment can modify surface chemistry, particularly when using monatomic ion beams such as Ar^+ to examine organic materials.[47] To reduce these effects, the ion beam energy was lowered to 500V while employing short cycling times to minimize localized artifacts from sputter induced heating.[48]

A sample depth profile of an annealed 5:3 blend film is shown in Figure 4, where several important features are noted.

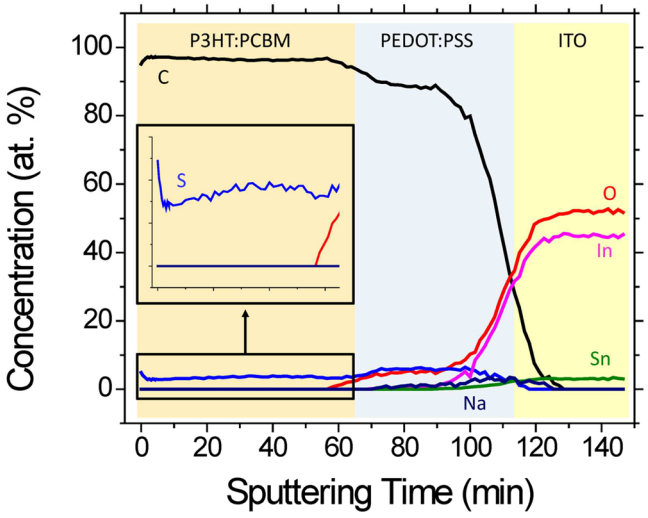

Figure 4. Depth profiling XPS results showing the elemental composition of an annealed P3HT:PCBM (5:3)/PEDOT:PSS/ITO film. Inset features a magnification of the low concentration elements found in the active layer film.

First, despite the significant oxygen concentration in PCBM (2.7 at. % based on chemical structure), negligible oxygen content was detected within the active layer, indicating preferential sputtering of the oxygenated moiety. Consequently, oxygen cannot be used to reliably track PCBM composition within the active layer. While measured oxygen content increases upon reaching the PEDOT:PSS interlayer, the observed concentration is still well below that predicted for a pristine PEDOT:PSS sample (~23 at %). This further confirms that oxygen content is preferentially removed from organics during low energy Ar^+ sputtering, so its usefulness as a barrier marker is also limited. However, carbon (expected in P3HT and PCBM) and sulfur (expected in P3HT and PEDOT:PSS) are observed at significant concentrations throughout the multilayer film, indicating that these elements may be used to track composition within the active layer.

Quantification of P3HT content throughout the active layer was carried out by comparing active layer sulfur:carbon ratios to those from a pure P3HT reference film subjected to identical sputtering conditions. However, deconvolution of PEDOT:PSS contributions to the overall elemental composition near the P3HT:PCBM/PEDOT:PSS interface remains challenging because the two blends have the same elemental constituents (C, S, and O), while the sharp interface transition is smeared by process variability (XPS probing depth and sputtering nonuniformity). To address this problem, high-resolution S 2p spectra were collected throughout the depth profiling experiments. The high resolution spectra retained contributions from both the sulfonate and thiophene groups found in PEDOT:PSS, though the relative peak area ratios were skewed

during sputtering when compared to a pristine PEDOT:PSS reference film. Quantification of the S 2p sulfonate component allowed selective removal of PEDOT:PSS contributions to both the measured C 1s and S 2p peak areas. These modified peak areas were then used to calculate the P3HT content of the active layer near the PEDOT:PSS interface. Further details regarding this procedure are found in the Supporting Information. Several P3HT content profiles were averaged together and are shown in Figure 5, where the film depth is normalized to account for film thickness variation.

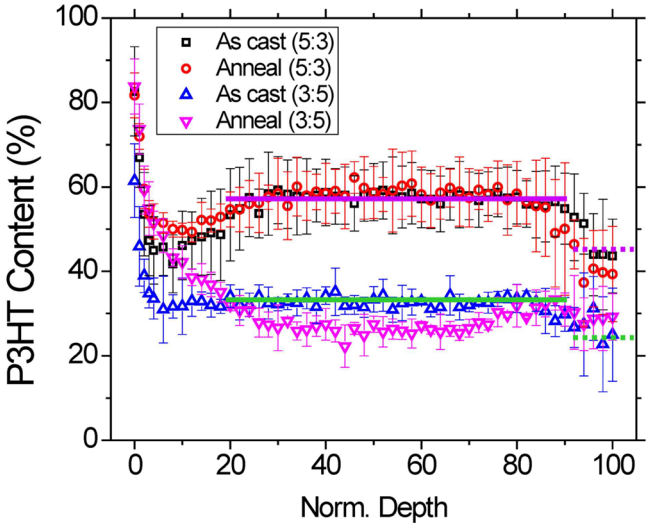

Figure 5. Calculated P3HT content within the as cast and annealed active layers with varying initial P3HT:PCBM blend ratios. The solid lines represent the predicted "bulk" composition for the 5:3 (purple) and 3:5 (green) P3HT:PCBM blends based solely on initial P3HT:PCBM concentration (58 and 33% P3HT, respectively). The square dot lines further take into account the predicted free energy difference for P3HT and PCBM deposition onto the PEDOT:PSS interlayer (46 and 24% P3HT for the 5:3 and 3:5 blends).

Several notable features are evident in the data as shown in Figure 5. First, the air interface is composed of a highly P3HT-enriched overlayer regardless of processing conditions and initial P3HT:PCBM concentration, although the cast 3:5 blend film shows lower P3HT surface content than the other blends. In the "bulk" film, the P3HT concentration reaches a plateau, which is strongly correlated to the initial blend concentration and matches predicted behavior. A slightly PCBM-rich interfacial layer, which is independent of annealing, is encountered at the PEDOT:PSS interface, in agreement with several works.[11,14,15,20] Interestingly, the buried interfacial composition is correlated to initial P3HT:PCBM concentration, yet the functional dependence on blend ratio is reduced due to the proximity of the PEDOT:PSS interlayer. Most importantly, in both cast and annealed samples, the active layer composition at the PEDOT:PSS interface matches that predicted by taking into account the free energy barrier for P3HT and PCBM deposition onto PEDOT:PSS. These findings clearly validate the presented interfacial energy framework as a simple method to predict the buried interfacial composition of a blended material on varying substrates, which is both difficult and time-consuming to address using traditional experimental methodology.

Additionally, the agreement between predicted profiles and experimentally derived profiles indicates for the first time that the vertical stratification within these films is largely dictated by thermodynamic considerations rather than kinetic limitations. Also supporting this conclusion is the strong similarity between the XPS depth profiles reported here and those profiles reported by Vaynzof et al.[15] despite their active layer being cast onto ZnO films using significantly different processing conditions (1:1 P3HT:PCBM, 35−48 mg/mL, 200−370 nm film thickness, annealed at 130 °C for 15 min). Another recent study also featured similar composition profiles to those presented herein after significantly extending annealing time (150 °C for 30 min vs 160 °C for 8 min in our work).[26] It is important to clarify that while the presented data and analysis suggest that the vertical concentration profile is thermodynamically stable, other structural changes may occur in the film upon additional annealing. Localized diffusion and molecular reorientation processes such as phase segregation, crystallization, and crystallite reorientation would still be expected to occur, leading to increased domain sizes and crystallite growth.[26,49] Longer range vertical concentration profiles, however, seem to be determined primarily from surface energy considerations (i.e., thermodynamic behavior) and are seemingly independent of extended annealing treatment.

As depicted in Figure 5, the region between the P3HT-rich air interface and the "bulk" region (*ca.* 5−20 nm normalized depth) features strong variation in measured concentration profiles, indicating some kinetic limitations during film casting. For the as cast 5:3 films, a slightly PCBM-rich sublayer is sandwiched between the P3HT-rich surface layer and the "bulk" film, though annealing seems to partially quench this sublayer. However, a similar PCBM-rich sublayer is not observed in the as cast 3:5 blend, which is discussed in more detail below. Annealing the 3:5 blend smoothes the sharp gradient from the exposed surface to the "bulk" film and produces a slight depression of the nominal "bulk" P3HT concentration. Each blend profile also features a rapid decrease in P3HT content just below the air interface, indicating that the P3HT-enriched capping layer could be thinner than the nominal XPS probing depth (~10 nm).

To further characterize blend composition near the air interface, ARXPS was performed on the various active layers (Figure 6). ARXPS is a nondestructive analytical technique where the sample surface is rotated relative to the detector in an effort to tune sampling depth (d) by adjusting photoelectron travel through the sample surface to the detector (Figure 6 inset). When the sample surface normal passes through the detector, a maximum sampling depth ($d_{max} = 3\lambda \approx 10$ nm) is achieved, accounting for 95% of the photoelectron signal. Sample rotation reduces sampling depth though the expression:[50]

$$d = 3\lambda \cos\theta \quad (5)$$

where λ and θ are the inelastic mean free path and photoelectron emission angle. By collecting spectra at different sample rotations, the surface sensitivity of XPS can be tuned, with higher emission angles probing shallower depths. The inelastic mean free paths of C 1s and S 2p photoelectrons (2.9 and 3.0 nm, respectively) were calculated from an empirical relation described elsewhere,[51] where blend density was estimated to be 1.3 g cm^{-3} based on P3HT and PCBM densities (1.1 and 1.5 g cm^{-3}).[7] Similar to depth profiling experiments, P3HT content was calculated from measured sulfur:carbon ratios compared to those observed for a pure P3HT film at identical emission angles. The calculated P3HT

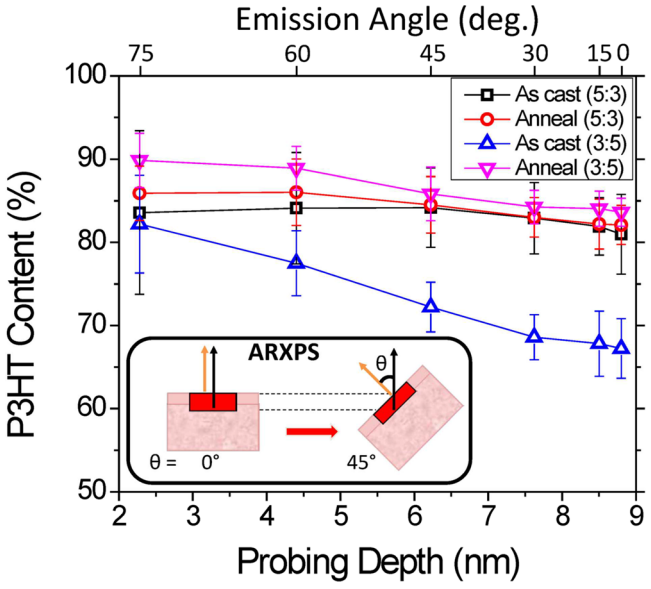

Figure 6. Calculated P3HT content near the exposed air surface as derived from ARXPS measurements. Each data point represents average P3HT content between the air surface (d = 0) and the effective probing depth (d = 3λcos θ). The secondary x-axis features emission angle (θ) used to derive probing depth where the conversion nonlinearity is evident. Inset features schematic diagram depicting ARXPS experimental setup where emitted photoelectrons (black arrows) travel the same distance through the film (dotted lines) before reaching the detector regardless of emission angle. The emission angle is defined as the angle between the emitted photoelectron's trajectory to the detector and the surface normal (orange arrows).

content (Figure 6) represents a convolution of composition throughout the entire sampling depth (i.e., from d = 0 to d = 3λcos θ), rather than the composition at one specific depth (d = 3λcos θ).

The ARXPS data reveal important features. The 5:3 blend films (both as cast and annealed) show composition independent of emission angle or probing depth, indicating that these surfaces feature uniform P3HT content and are thermodynamically stable. In contrast, the as cast 3:5 blend film displays a steady decline in P3HT content with increased probing depth, while the topmost surface layer features composition consistent with the 5:3 films. Annealing the 3:5 films resulted in enriched P3HT composition profiles comparable to those observed for the 5:3 blend films. Interestingly, a pure P3HT capping layer is not detected despite the appreciable difference in surface energies, though this is consistent with the presence of PCBM clusters observed by AFM phase imaging. If a pure P3HT surface layer does exist, its thickness must be < 2 nm, and would thus be convoluted in the ARXPS data with the blended region sublayers.

When coupled with the depth profiling data, the 3:5 blend ARXPS data strongly suggest that P3HT migrates toward (or conversely, PCBM migrates away from) the air interface during annealing to yield a thermodynamically stable, P3HT-enriched overlayer. The same behavior is seen in the 5:3 blend depth profiles, where a pronounced PCBM-rich sublayer is detected in the as cast film. Because the 5:3 blend features a higher P3HT concentration, the P3HT-rich overlayer is constructed rapidly during solvent drying, necessitating only localized diffusion. During annealing, P3HT from the "bulk" region mobilizes to diminish the localized PCBM-rich sublayer. In contrast, the 3:5 blend has appreciably lower P3HT content throughout the film and is therefore able to form only a very thin, incomplete P3HT-rich overlayer before drying. Upon annealing, P3HT from the "bulk" region again diffuses toward the air interface to increase P3HT content in the overlayer, but the limited P3HT content in the "bulk" reservoir results in P3HT content reduction throughout the bulk of the active layer. Thus, after annealing, vertical stratification within the entire active layer is influenced by interfacial phenomena for the 3:5 blend ratio, while interface effects are limited to ∼30% of the total 5:3 film thickness.

CONCLUSIONS

Vertical composition profiles within fabricated P3HT:PCBM bulk heterojunction active layers were predicted using the acid−base surface energy model coupled with contact angle measurements using several high-energy solvents. From this comprehensive free energy approach, the thermodynamically favored P3HT:PCBM blend consists of a uniformly blended "bulk" region sandwiched between a P3HT-rich air interface and a PCBM-rich buried interface. Although the P3HT-rich interface is independent of initial P3HT:PCBM ratio, the "bulk" and buried interface are strongly correlated with this parameter though the buried interface composition is skewed by repulsive interactions with the underlying PEDOT:PSS layer.

As experimental verification, low energy depth profiling with XPS and ARXPS was performed. Depth profiles conclusively showed that P3HT diffuses toward the surface during annealing. Also noted was the emergence of a PCBM-rich sublayer below the P3HT-rich air interface in the as cast films, which appears to be a kinetic construct as annealing reduces its prevalence. Overall, experimentally derived depth profiles between as cast and annealed blend films closely matched predicted behavior, verifying that the measured vertical stratification is thermodynamically driven. These results further suggest that careful control over processing conditions such as solvent choice and substrate surface properties could be tuned to tailor the resulting vertical phase segregation and thereby improve device performance. Furthermore, the robustness of the comprehensive free energy approach in predicting interfacial composition within active layer films is validated, allowing more detailed understanding of substrate effects on interfacial behavior without time-consuming and complex experimental probing. Such understanding is essential for predicting structurally integrated device compatibility and will likely be broadly applicable to additional systems containing low band gap polymers, ternary blends, and small molecule devices.

ASSOCIATED CONTENT

Supporting Information

A detailed explanation regarding theoretical background of surface energy acid−base theory with accompanying parameters for probe liquids, wettability measurements, surface energy parameter extraction, and P3HT content extraction from XPS depth profiles and ARXPS along with AFM images and calculated free energies. This material is available free of charge via the Internet at http://pubs.acs.org.

AUTHOR INFORMATION

Corresponding Author

*E-mail: Benjamin.Leever@wpafb.af.mil. Tel.: +01 1937 255 9141. Fax: +01 1937 656 6327 .

Notes

The authors declare no competing financial interest.

ACKNOWLEDGMENTS

The authors thank S. Apt and R. Wheeler at the Air Force Research Laboratory's Materials Characterization Facility for their assistance with FIB and TEM processing. This work was funded by the Air Force Office of Scientific Research.

REFERENCES

(1) Myers, J. D.; Xue, J. *Polymer Rev.* **2012**, *52*, 1−37.
(2) Brady, M. A.; Su, G. M.; Chabinyc, M. L. *Soft Matter* **2011**, *7*, 11065−11077.
(3) Liu, F.; Gu, Y.; Jung, J. W.; Jo, W. H.; Russell, T. P. *J. Polym. Sci., Part B: Polym. Phys.* **2012**, *50*, 1018−1044.
(4) Kim, Y.; Ballantyne, A. M.; Nelson, J.; Bradley, D. D. C. *Org. Electron.* **2009**, *10*, 205−209.
(5) Campoy-Quiles, M.; Ferenczi, T.; Agostinelli, T.; Etchegoin, P. G.; Kim, Y.; Anthopoulos, T. D.; Stavrinou, P. N.; Bradley, D. D. C.; Nelson, J. *Nat. Mater.* **2008**, *7*, 158−164.
(6) Germack, D. S.; Chan, C. K.; Kline, R. J.; Fischer, D. A.; Gundlach, D. J.; Toney, M. F.; Richter, L. J.; DeLongchamp, D. M. *Macromolecules* **2010**, *43*, 3828−3836.
(7) van Bavel, S. S.; Sourty, E.; With, G. d.; Loos, J. *Nano Lett.* **2009**, *9*, 507−513.
(8) van Bavel, S. S.; Bärenklau, M.; de With, G.; Hoppe, H.; Loos, J. *Adv. Funct. Mater.* **2010**, *20*, 1458−1463.
(9) Moon, J. S.; Lee, J. K.; Cho, S.; Byun, J.; Heeger, A. J. *Nano Lett.* **2008**, *9*, 230−234.
(10) Ruderer, M. A.; Guo, S.; Meier, R.; Chiang, H.-Y.; Körstgens, V.; Wiedersich, J.; Perlich, J.; Roth, S. V.; Müller-Buschbaum, P. *Adv. Funct. Mater.* **2011**, *21*, 3382−3391.
(11) Parnell, A. J.; Dunbar, A. D. F.; Pearson, A. J.; Staniec, P. A.; Dennison, A. J. C.; Hamamatsu, H.; Skoda, M. W. A.; Lidzey, D. G.; Jones, R. A. L. *Adv. Mater.* **2010**, *22*, 2444−2447.
(12) Xue, B.; Vaughan, B.; Poh, C.-H.; Burke, K. B.; Thomsen, L.; Stapleton, A.; Zhou, X.; Bryant, G. W.; Belcher, W.; Dastoor, P. C. *J. Phys. Chem. C* **2010**, *114*, 15797−15805.
(13) Wang, H.; Gomez, E. D.; Kim, J.; Guan, Z.; Jaye, C.; Fischer, D. A.; Kahn, A.; Loo, Y.-L. *Chem. Mater.* **2011**, *23*, 2020−2023.
(14) Germack, D. S.; Chan, C. K.; Hamadani, B. H.; Richter, L. J.; Fischer, D. A.; Gundlach, D. J.; DeLongchamp, D. M. *Appl. Phys. Lett.* **2009**, *94*, 233303.
(15) Vaynzof, Y.; Kabra, D.; Zhao, L.; Chua, L. L.; Steiner, U.; Friend, R. H. *ACS Nano* **2011**, *5*, 329−336.
(16) Yu, B.-Y.; Lin, W.-C.; Wang, W.-B.; Iida, S.-i.; Chen, S.-Z.; Liu, C.-Y.; Kuo, C.-H.; Lee, S.-H.; Kao, W.-L.; Yen, G.-J.; You, Y.-W.; Liu, C.-P.; Jou, J.-H.; Shyue, J.-J. *ACS Nano* **2010**, *4*, 833−840.
(17) Wang, D. H.; Lee, H. K.; Choi, D.-G.; Park, J. H.; Park, O. O. *Appl. Phys. Lett.* **2009**, *95*, 043505.
(18) Jo, J.; Na, S.-I.; Kim, S.-S.; Lee, T.-W.; Chung, Y.; Kang, S.-J.; Vak, D.; Kim, D.-Y. *Adv. Funct. Mater.* **2009**, *19*, 2398−2406.
(19) Björström, C. M.; Bernasik, A.; Rysz, J.; Budkowski, A.; Nilsson, S.; Svensson, M.; Andersson, M. R.; Magnusson, K. O.; Moons, E. *J. Phys.: Condens. Matter* **2005**, *17*, L529−L534.
(20) Xu, Z.; Chen, L.-M.; Yang, G.; Huang, C.-H.; Hou, J.; Wu, Y.; Li, G.; Hsu, C.-S.; Yang, Y. *Adv. Funct. Mater.* **2009**, *19*, 1227−1234.
(21) Kim, Y. S.; Lee, Y.; Kim, J. K.; Seo, E.-O.; Lee, E.-W.; Lee, W.; Han, S.-H.; Lee, S.-H. *Curr. Appl. Phys.* **2010**, *10*, 985−989.
(22) Yao, Y.; Hou, J.; Xu, Z.; Li, G.; Yang, Y. *Adv. Funct. Mater.* **2008**, *18*, 1783−1789.
(23) Wu, F.-C.; Huang, Y.-C.; Cheng, H.-L.; Chou, W.-Y.; Tang, F.-C. *J. Phys. Chem. C* **2011**, *115*, 15057−15066.
(24) Chiu, M.-Y.; Jeng, U. S.; Su, M.-S.; Wei, K.-H. *Macromolecules* **2009**, *43*, 428−432.
(25) Treat, N. D.; Shuttle, C. G.; Toney, M. F.; Hawker, C. J.; Chabinyc, M. L. *J. Mater. Chem.* **2011**, *21*, 15224−15231.
(26) Chen, D.; Nakahara, A.; Wei, D.; Nordlund, D.; Russell, T. P. *Nano Lett.* **2010**, *11*, 561−567.
(27) Johnson Jr, R. E.; Dettre, R. H. In *Surface and Colloid Science*; Matijevic, E., Ed.; Wiley Interscience: New York, 1969; Vol. 2, pp 85−153.
(28) Ma, K.-X.; Ho, C.-H.; Zhu, F.; Chung, T.-S. *Thin Solid Films* **2000**, *371*, 140−147.
(29) Berg, J. C. *An Introduction to Interfaces & Colloids: The Bridge to Nanoscience*, 1st ed.; World Scientific Publishing: Hackensack, NJ, 2010.
(30) Oh, J. Y.; Jang, W. S.; Lee, T. I.; Myoung, J.-M.; Baik, H. K. *Appl. Phys. Lett.* **2011**, *98*, 023303.
(31) Van Oss, C. J. *Interfacial Forces in Aqueous Media*, 2nd ed.; CRC Press: Boca Raton, FL, 2006.
(32) Kim, J. S.; Friend, R. H.; Cacialli, F. *J. Appl. Phys.* **1999**, *86*, 2774−2778.
(33) Zhong, Z. Y.; Jiang, Y. D. *J. Colloid Interface Sci.* **2006**, *302*, 613−619.
(34) Lee, E. S.; Choi, J. H.; Baik, H. K. *Surf. Coat. Technol.* **2007**, *201*, 4973−4978.
(35) Jung, M.-H.; Choi, H.-S. *J. Colloid Interface Sci.* **2007**, *310*, 550−558.
(36) Bianchi, R. F.; Carvalho, A. J. F.; Pereira-da-Silva, M. A.; Balogh, D. T.; Faria, R. M. *Mater. Sci. Eng., C* **2004**, *24*, 595−599.
(37) Chen, J.-J.; Struk, K. N.; Brennan, A. B. *Langmuir* **2011**, *27*, 13754−13761.
(38) Ucar, I. O.; Doganci, M. D.; Cansoy, C. E.; Erbil, H. Y.; Avramova, I.; Suzer, S. *Appl. Surf. Sci.* **2011**, *257*, 9587−9594.
(39) Mohan, T.; Kargl, R.; Doliška, A.; Vesel, A.; Köstler, S.; Ribitsch, V.; Stana-Kleinschek, K. *J. Colloid Interface Sci.* **2011**, *358*, 604−610.
(40) Ma, X.; Wigington, B.; Bouchard, D. *Langmuir* **2010**, *26*, 11886−11893.
(41) Clark, M. D.; Krishnamoorti, R. *J. Phys. Chem. C* **2009**, *113*, 20861−20868.
(42) Davenas, J.; Besbes, S.; Abderrahmen, A.; Jaffrezic, N.; Ben Ouada, H. *Thin Solid Films* **2008**, *516*, 1341−1344.
(43) Wang, X.; Ederth, T.; Inganäs, O. *Langmuir* **2006**, *22*, 9287−9294.
(44) Han, Y.-K.; Chang, M.-Y.; Huang, W.-Y.; Pan, H.-Y.; Ho, K.-S.; Hsieh, T.-H.; Pan, S.-Y. *J. Electrochem. Soc.* **2011**, *158*, K88−K93.
(45) Vacca, P.; Petrosino, M.; Miscioscia, R.; Nenna, G.; Minarini, C.; Della Sala, D.; Rubino, A. *Thin Solid Films* **2008**, *516*, 4232−4237.
(46) Chang, L.; Lademann, H. W. A.; Bonekamp, J.-B.; Meerholz, K.; Moulé, A. J. *Adv. Funct. Mater.* **2011**, *21*, 1779−1787.
(47) Wagner, T.; Wang, J. Y.; Hofman, S. In *Surface Analysis by Auger and X-Ray Photoelectron Spectroscopy*; Briggs, D., Grant, J. T., Eds.; IM Publications: Chichester, U.K., 2003; pp 619−649.
(48) Baer, D. R.; Gaspar, D. J.; Engelhard, M. H.; Lea, A. S. In *Surface Analysis by Auger and X-Ray Photoelectron Spectroscopy*; Briggs, D., Grant, J. T., Eds.; IM Publications: Chichester, U.K., 2003; pp 211−234.
(49) Yang, F.; Forrest, S. R. *ACS Nano* **2008**, *2*, 1022−1032.
(50) Cumpson, P. J. In *Surface Analysis by Auger and X-Ray Photoelectron Spectroscopy*; Briggs, D., Grant, J. T., Eds.; IM Publications: Chichester, U.K., 2003; pp 651−675.
(51) Ratner, B. D.; Castner, D. G. In *Surface Analysis−The Principle Techniques*, 2nd ed.; Vickerman, J. C., Gilmore, I. S., Eds.; John Wiley & Sons: Chichester, U.K., 2009; pp 47−112.